UC Davis
UC Davis Previously Published Works

Title

Performance of high-resolution CT for detection and discrimination tasks related to stenotic lesions - A phantom study using model observers.

Permalink

https://escholarship.org/uc/item/05h2d061

Journal

Medical Physics, 50(4)

Authors

Hernandez, Andrew
Burkett, George
Pham, Nancy
et al.

Publication Date

2023-04-01

DOI

10.1002/mp.16194

Peer reviewed

eScholarship.org Powered by the California Digital Library
University of California

Author Manuscript

Author Manuscript

Author Manuscript

Author Manuscript

HHS Public Access

Author manuscript

Med Phys. Author manuscript; available in PMC 2024 August 12.

Published in final edited form as:

Med Phys. 2023 April ; 50(4): 2037–2048. doi:10.1002/mp.16194.

Performance of high-resolution CT for detection and discrimination tasks related to stenotic lesions - a phantom study using model observers

Andrew M. Hernandez[1], **George W. Burkett**[1], **Nancy Pham**[2], **Craig K. Abbey**[3], **John M. Boone**[1,4]

[1]Department of Radiology, University of California Davis, Sacramento, CA, 95817

[2]Department of Radiology, University of California Los Angeles, Los Angeles, CA, 90095

[3]Department of Psychological & Brain Sciences, University of California Santa Barbara, Santa Barbara, CA, 93106

[4]Department of Biomedical Engineering, University of California Davis, Davis, CA, 95616

Abstract

Background: Accurate detection and grading of atheromatous stenotic lesions within the cardiac, renal, and intracranial vasculature is imperative for early recognition of disease and guiding treatment strategies.

Purpose: In this work, a stenotic lesion phantom was used to compare high resolution and normal resolution modes on the same CT scanner in terms of detection and size discrimination performance.

Materials and Methods: The phantom is comprised of three acrylic cylinders (each 15.0 cm in diameter and 1.3 cm thick) with a matching array of holes in each module. The outer two modules contain holes that are slightly larger than the corresponding hole in the central module to simulate stenotic narrowing in vasculature. The stack of modules was submerged in an iodine solution simulating contrast-enhanced stenotic lesions with a range of lumen diameters (1.32 mm to 10.08 mm) and stenosis severity (0, 50%, 60%, 70%, and 80%). The phantom was imaged on the Canon Aquilion Precision high-resolution CT scanner in high-resolution (HR) mode (0.25 mm × 0.50 mm detector element size) and normal-resolution (NR) mode (0.50 mm × 0.50 mm) using 120 kV and two dose levels (14 and 21 mGy SSDE) with 30 repeat scans acquired for each combination. Filtered back-projection (FBP) and a hybrid-iterative reconstruction (AIDR) were used with the FC18 kernel, as well as a deep learning algorithm (AiCE) which is only available for HR. A non-prewhitening model observer with an eye filter was implemented to quantify performance for detection and size discrimination tasks in the axial plane.

CONFLICT OF INTERESTS

Author J.M.B. is a director and shareholder in Izotropic Corporation. Authors C.K.A. and A.M.H. are consultants for Izotropic Corporation.The research was also supported in part by a research grant No. R01 EB025829 from the National Institute of Biomedical Imaging and Bioengineering, and a research grant No. R01 CA181081 from the National Cancer Institute. In his role as editor-in chief for Medical Physics, author J.M.B. was blinded to the review process and had no role in decisions pertaining to this manuscript.

Author Manuscript Author Manuscript Author Manuscript Author Manuscript

Results: Detection performance improved with increasing diameter, dose, and for AIDR in comparison to FBP for a fixed resolution mode. Performance in the HR mode was generally higher than NR for the smaller lumen diameters (1–5 mm) with decreasing differences as the diameter increased. Performance in NR mode surpassed HR mode for lumen diameters greater than ~4 mm and ~5 mm for 14 mGy and 21 mGy, respectively. AiCE provided consistently higher detection performance compared with AIDR-FC18 (48% higher for a 6 mm lumen diameter). Discrimination performance increased with increasing nominal diameter, dose, and for larger differences in stenosis severity. When comparing discrimination performance in HR to NR modes, the largest relative differences occur at the smallest nominal diameters and smallest differences in stenosis severity. The AiCE reconstruction algorithm produced the highest overall discrimination performance values, and these were significantly higher than AIDR-FC18 for nominal diameters of 7.14 and 10.08 mm.

Conclusions: HR mode outperforms NR for detection up to a specific diameter and the results improve with AiCE and for higher dose levels. For the task of size discrimination, HR mode consistently outperforms NR if AIDR-FC18 is used for dose levels of at least 21 mGy, and the results improve with AiCE and for the smallest differences in stenosis severity investigated (50% vs. 60%). High-resolution CT appears to be beneficial for detecting smaller simulated lumen diameters (<5 mm) and is generally advantageous for discrimination tasks related to stenotic lesions, which inherently contain information at higher frequencies, given the right reconstruction algorithm and dose level.

1. INTRODUCTION

Accurate detection and grading of stenotic lesions are imperative for early recognition of atherosclerotic disease and guiding treatment strategies.[1,2] Several methods for the quantification of carotid stenosis were used in the early 1990s in large-randomized trials (North American Symptomatic Carotid Endarterectomy Trial Collaborators[3] “NASCET’ and the European Carotid Surgery Trialists’ Collaborative Group[4] “ECST”). These relied on indirect ratio methods given that direct methods were not possible with conventional imaging modalities of that time (i.e., catheter angiography and digital subtraction imaging). Direct methods for renal and carotid stenosis assessment are now possible with advances in computed tomography (CT) and magnetic resonance (MR) imaging.[5–8] – making carotid stenosis assessment using CT angiography (CTA) or MR angiography (MRA) now standard practice in the clinic[1,9,10]. Carotid endarterectomy, a surgical procedure employed to reduce the risk of stroke from carotid artery stenosis[11], is highly beneficial in patients with 70% stenosis or greater without near occlusion - resulting in a 16% decrease in the 5-year risk of an ipsilateral stroke.[12]. For patients with 50–69% stenosis the benefit of endarterectomy is marginal, and for patients with <50% stenosis no positive effect is seen with surgery.[12] The clear dependency of carotid stenosis grading on the efficacy of treatment, underlines the need for accurate and precise measurements of stenosis severity. In other words, the ability to distinguish between a 60% and 70% stenosis is imperative for deciding on whether to use surgery for treatment.

The grading of stenotic lesions is related to the perceptual task of discriminating physical size differences between separate features of the CT image. Discriminating a more occluded

Author Manuscript Author Manuscript Author Manuscript Author Manuscript

lumen from a less occluded one is an integral part of lesion characterization. In much the same way that image noise can limit the detectability of some anatomical object of interest, noise can also limit the ability to distinguish between objects with different physical features of interest (e.g., size, shape, and contrast).[13–16] Both detection and discrimination tasks may be relevant for assessing imaging methodologies in a more clinical context such as assessment of vascular stenoses. At a more fundamental level, these different tasks often emphasize different spatial frequencies. For detection of a contiguous region of increased or decreased attenuation (e.g., a vascular lumen), the largest frequency components are often found at low spatial frequencies. For tasks such as discriminating a slightly larger lumen from a smaller one, the lower spatial frequencies are often similar, and the largest differences in the spectra are found at higher frequencies.

High-resolution CT (HRCT) scanners offer the ability to produce images with a greater range of frequency content. The purpose of this work is to assess relative performance of detection and discrimination tasks for comparing high resolution mode with normal resolution mode on the same system. We expect comparable performance in detection tasks for high resolution and normal resolution modes since the relevant frequencies are typically lower, but improved performance in the discrimination tasks that emphasize higher spatial frequencies. We designed and built a phantom that is representative of simple luminal stenosis detection and discrimination tasks with luminal diameter size ranges (1.32 mm to 10.08 mm) that are relevant to intracranial, coronary, and renal stenoses.[17–19]

2. METHODS

2.1. Stenotic lesion phantom design

A phantom was designed for simulating atheromatous luminal stenoses in contrast-enhanced CT examinations, hereafter referred to as the “stenosis phantom.” The phantom is comprised of three acrylic cylinders each 15.0 cm in diameter and 1.3 cm thick. Each module contains a matching array of holes at three different radial locations – 6 holes at a radial distance of 1.9 cm from the central axis of the phantom (R_A), 12 holes at 3.8 cm (R_B), and 24 holes at 6.4 cm (R_C) as shown in Figure 1a. Each hole was first drilled out using a slightly smaller sized bit followed by a precision reamer. This method produces highly accurate holes with smooth side walls. The two outer modules have identical sized holes, and the central module contains holes that are smaller in diameter simulating an arterial stenosis. Table 1 outlines the array of different nominal diameters ($D_{nominal}$) used in specifying each hole size. For example, hole index #9 has a 1.85 mm simulated lumen diameter in the outer disk and a 1.61 mm lumen diameter in the central disk emulating a 2.95 mm nominal lesion with a 60% and 70% stenosis severity, respectively. The term “simulated-lumen diameter” will hereafter be referred to as simply “lumen diameter”. Stenosis severity is defined as the reduction in cross-sectional area of the lumen reported herein as a percentage. The phantom was designed to have several repeat lumen diameters and stenosis gradings within the inner most radial locations (R_A and R_B) as detailed in Table 1. The purpose of this was to investigate the effect of spatial location within the phantom (and system geometry) to see if there were any observable differences in detectability performance.

Author Manuscript Author Manuscript Author Manuscript Author Manuscript

For aligning the central axes of the modules, a 0.51 cm hole was machined through all three modules and fastened using Nylon all-thread, washers, and nuts. A centering pin was placed in one of the stenosis hole-pairs for fine alignment. Once aligned, the nuts were then tightened to lock in alignment and minimize air gaps between each module. The stack of acrylic cylinders was then placed within a water-tight polyethylene container that is 19.1 cm in length and tapers in diameter from 19.1 cm at the top to 15.9 cm at the bottom. To minimize the volume of iodine solution that is required to fill the 1-gallon container and to minimize the chance of air bubbles, several acrylic disks were placed immediately above and below the stack of stenosis modules – positioning the stack approximately in the center (along z) of the container. These two regions (above and below the stack) mimic continuous scatter media encountered in a clinical CT exam. The two regions were filled with wax pellets and partitioned from the stenotic lesion region using a mesh screen. The mesh screen contains holes that are small enough to stop the pellets from passing through and potentially getting into the stenosis hole pairs, but big enough to easily allow the iodine solution to complete diffuse through the phantom and fill the hole pairs.

The phantom container was filled with ~10 mg/ml of iodine solution which was prepared by serial dilution of Visipaque™ and distilled water. This specific iodine concentration was chosen to simulate a contrast of ~130 HU with respect to the acrylic background consistent with the lower range of contrast enhancement thresholds recommended for stenotic lesions throughout the body.[20–22] The relationship between HU and iodine concentration was determined *a priori* by scanning a custom iodine calibration phantom, previously reported[23], on the Aquilion Precision (Canon Medical Systems, Otawara, Japan) high-resolution CT scanner (explained in detail in the following section) at 120 kV. The calibration phantom is composed of small plugs of iodine of various concentrations (0, 2, 5, 10, 15 and 20 mg/cc iodine) all encased within a thin plastic rod (CIRS Inc., Norfolk, VA). The calibration phantom was placed within the 32 cm CTDI phantom and scanned at maximum mAs resulting in CT numbers of 274.5 HU for the 10 mg/ml iodine slug and 140.5 HU for the acrylic background. The CT number of the ~10 mg/ml iodine solution in the stenosis phantom was measured by placing two regions of interest (ROIs) in the central slice of an outer module within the largest lumen diameter near the center and at the periphery of the phantom (i.e. hole index #20 at radial locations R_A and R_C from Table 1). The mean CT number within the two ROIs were within 3% of each other and the average of the two was measured to be 263.8 HU. The CT number for the acrylic bulk material was measured using identical sized ROIs as the iodine measurement and ROI locations directly adjacent to the iodine measurement. The mean CT number within the two acrylic ROIs were within 1% of each other and the average of the two was measured to be 139.5 HU. All ROI measurements were made in the CT volume data set with a nominal reconstruction protocol (120 kV, FBP-FC18). A final image contrast of 124 HU (rounded to the nearest integer) was measured for the simulated stenotic lesions.

2.2. Phantom Imaging and Reconstruction

The stenosis phantom was positioned in the Aquilion Precision HRCT scanner with care taken to align the phantom in the axial plane. A collimation width of 4 cm was used to cover the z-extent of the stenosis phantom modules (3.9 cm in total) in a single axial rotation

Author Manuscript Author Manuscript Author Manuscript Author Manuscript

(i.e., no table motion), and the phantom was scanned in both normal resolution "NR" mode (0.50 mm × 0.50 mm detector element size in the channel and row directions, respectively) and high-resolution "HR" mode (0.25 mm × 0.50 mm detector element size) using 120 kV. Depending on the specified dose of the scan, gantry rotation times of 0.5 or 0.6 seconds and either of the two smallest focal spot sizes (0.4 × 0.5 mm and 0.6 × 0.6 mm) were used. The large (body) bowtie filter was used for all acquisitions, but as previously reported[24] the body bowtie filter for HR mode is less attenuating than the corresponding filter used for NR mode resulting in ~23% higher $CTDI_{vol,32}$ values for HR compared with NR mode at the same mAs. To compensate for this, higher mAs values were used for NR mode than for HR mode, and the mAs values were selected to deliver two different $CTDI_{vol,32}$ values of 7 mGy and 11 mGy (rounded to the nearest integer) as provided by the system. The adult body $CTDI_{vol,32}$ to size-specific dose estimate (SSDE) conversion factors from AAPM Report 204[25] were then used to compute the corresponding SSDE levels of 14 mGy and 21 mGy (rounded to the nearest integer). This range of SSDE levels is consistent with published diagnostic reference levels (DRLs) for abdomen and pelvis CT examinations with contrast[26]. If $CTDI_{vol,16}$ values and head $CTDI_{vol,16}$-to-SSDE conversation factors from AAPM Report 293[27] were used instead, albeit with the body bowtie filter as was used in the acquisitions, the resulting SSDE levels range from 9 mGy to 18 mGy which encompasses the published DRL of 16.5 mGy SSDE (converted from 18 mGy $CTDI_{vol}$ published in Table 4 of reference) for neck CT examinations with contrast.[26] A water equivalent diameter (D_w) of 18.6 cm was used for all SSDE calculations. Thirty repeat scans were acquired for the two dose levels and two resolution modes (120 total scans) for use in detectability estimation.

For all phantom acquisitions, the image data were reconstructed using FBP and a hybrid-iterative (AIDR3D Standard) reconstruction algorithm, hereafter termed "AIDR", with the FC18 "Body" kernel. For only the HR mode acquisitions, the Advanced Intelligent Clear-IQ Engine (AiCE) deep learning reconstruction, specifically designed for the body (AiCE Body), was used at two levels (Standard and Strong) – hereafter referred to as AiCE-STD and AiCE-STR. AiCE-STR was used only for the 14 mGy SSDE scans as this "strong" denoising is designed to benefit lower dose applications and is of less interest at 21 mGy where it is expected that all AiCE reconstructions will perform well. AiCE is currently not available for use with NR mode acquisitions. A reconstruction diameter of 400 mm and a slice thickness of 0.5 mm was used for all reconstructions resulting in voxel sizes of 0.78 mm × 0.78 mm × 0.50 mm for NR mode (512 × 512 matrix size) and 0.39 mm × 0.39 mm × 0.50 mm for HR (1024 × 1024).

2.3. Detectability

Detection and size discrimination were estimated for axial slices extracted from the 3D CT volume using the non-prewhitening model observer[28] with an eye filter[29] (NPWE) as described in detail in the follow two sections. Each hole pair in the phantom was first localized in the ensemble average volume of all 30 repeat scans. Slices containing air bubbles or the interface between an outer and central module were excluded from the analysis resulting in 21 slices per module (63 slices total). Regions-of-interest (ROIs) with a spatial extent in the axial plane equal to 1.5 times the lumen diameter were extracted for all

Author Manuscript Author Manuscript Author Manuscript Author Manuscript

lumens in the phantom and a circular Hough transform was used to estimate the position of the center of each lumen.

2.3.1. Detection—The detection template, $\boldsymbol{w}$ a N × N array, required for implementation of the NPWE model was synthesized using the known lumen diameters and measured image contrast (124 HU), blurred by the axial plane MTF, and convolved with the square of the eye filter. The MTF was measured on the Aquilion Precision, using a previously reported method[30], across the range of radial distances from the isocenter, focal spot sizes, gantry rotation times, resolution modes, voxels sizes, and reconstruction algorithms/kernels explored in this work. The axial plane MTF was assumed to be isotropic in (f_x and f_y) which is a reasonable assumption given that all lumens are relatively close to the isocenter and therefore similarly affected by azimuthal and radial blur.[30] All lumens in the first two radial arrays (R_A = 1.9 cm and R_B = 3.8 cm) were blurred using the MTF measured at a radial distance of 4 cm from the scanner isocenter and the lumens in the outer array (R_C = 6.4cm) were blurred using the axial MTF measured at a radial distance of 7.5 cm. This step takes into account a relatively small, but observable decrease in the MTF (at least in HR mode) as previously described.[30] We utilized an eye filter, $\boldsymbol{E}$, proposed by Burgess[29] to include contrast sensitivity of the human visual system with "c" the exponential parameter set to 2.2 for a typical viewing distance of 50 cm.

Template responses were computed as the inner product of w with the N × N ROI from the CT volume. The signal-present response, $\lambda^{+}_{i,j}$, was computed as the inner product of w with the CT ROI at the slice index i, where $i = 1, \ldots, 21$ indexes the 21 slices for the central and outer modules, and index j represents the 30 repeat scans. A non-signal location adjacent to the target location was used to form the signal-absent response $\lambda^{-}_{i,j}$ across the module slices and repeat scans. The average signal-present and signal-absent template responses are represented by $\overline{\lambda}^{+}$ and $\overline{\lambda}^{-}$, respectively. Signal-present variance, $\widehat{\sigma}^2_{\lambda^+}$, was computed as the sample variance of the signal-present responses, and the signal-absent variance, $\widehat{\sigma}^2_{\lambda^-}$, was computed as the sample variance of the signal-present response. The resulting detectability estimation is then given by,

$$d'_{det} = \frac{\overline{\lambda}^{+} - \overline{\lambda}^{-}}{\sqrt{\frac{1}{2}\left(\widehat{\sigma}^2_{\lambda^+} + \widehat{\sigma}^2_{\lambda^-}\right)}}. \tag{1}$$

Detection performance (d'_{det}) was calculated separately for the 84 holes of various diameters (42 in the outer module and 42 in the central modules). Bootstrapping over the 30 replicate CT scans with 1000 resamples (including replication) was used to derive error in the d'_{det} estimation. Detectability estimates were calculated separately for each dose level, resolution mode and reconstruction algorithm/kernel combination. In addition, the ratio of HR mode to NR mode results was analyzed as a function of lumen diameter. To obtain a lumen-diameter threshold for which there is an expected advantage for HR mode (denoted as $D_{HR>NR}$), we fit a line to the data for all diameters (except 10.08 mm) and evaluated the diameter at which the line has a value of 1. The error in the $D_{HR>NR}$ estimation was derived

Author Manuscript Author Manuscript Author Manuscript Author Manuscript

from bootstrapping over the range of lumen diameters with 1000 resamples (including replication).

2.3.2. Size Discrimination—The detection template, $\boldsymbol{w}$, for the size discrimination task was synthesized as the difference between the outer module lumen diameter and the central module lumen diameter. Referring to Figure 1b and Table 1, the index location 1 represents the task of discriminating between a 50% stenosis (2.08 mm diameter lumen in outer module) and a 70% stenosis (1.61 mm lumen in central module) for a nominal lumen diameter of 2.95 mm. The signal present response, $\lambda^{+}_{i,j}$, was computed as the inner product of $\boldsymbol{w}$ with the CT ROI for the outer module (i.e., larger lumen diameter) at the slice index i and scan index j. The signal-absent response, $\lambda^{-}_{i,j}$, was computed as the inner product of $\boldsymbol{w}$ with the CT ROI for the central module (i.e., smaller lumen diameter) at the slice index i and scan index j. Signal-absent and signal-present variance was estimated as described in the previous section. Given these definitions of the signal response and variance, detectability for the size discrimination task, d'_{dis}, is then given by,

$$d'_{dis} = \frac{\bar{\lambda}^{+} - \bar{\lambda}^{-}}{\sqrt{\frac{1}{2}\left(\hat{\sigma}^{2}_{\lambda^{+}} + \hat{\sigma}^{2}_{\lambda^{-}}\right)}}. \tag{2}$$

Discrimination performance was calculated separately for the 42 hole-pair combinations (24 of which are the unique combinations detailed in Table 1). Error in the d'_{dis} estimation was derived by bootstrapping over the 30 replicate scans with 1000 resamples (with replication). Detectability estimations were performed separately for each dose level, resolution mode and reconstruction algorithm/kernel combination.

3. RESULTS

Figure 2 shows example axial slices through the outer and central stenosis modules as well as coronal slices through several modeled stenotic lesions. The phantom modules are surrounded by iodine solution resulting from the radial gap between the outer diameter of the modules and the inner diameter of the polyethylene phantom container. The air region near the top of the phantom is due to the phantom volume not being 100% filled.

An example of the difference signal for the detection task (signal present – signal absent) and the corresponding Fourier transform are shown in Figures 3a and 3b, respectively, for a 7.14 mm lumen diameter. From this example it can be observed that the spectrum is concentrated at low spatial frequencies, 95% of the signal intensity is less than 0.35 mm^{-1}. The corresponding difference signal and Fourier transform for the discrimination task are shown in Figures 3c and 3d, respectively, representing the difference between a 50% and 70% stenosis for a 7.14 mm nominal lumen diameter. Notice the largest differences in the spectra are found at high frequencies. Now the signal spectrum is spread across a broader range of spatial frequencies with 95% of the signal intensity less than 0.58 mm^{-1}.

Author Manuscript Author Manuscript Author Manuscript Author Manuscript

3.1. Detection

Detection performance for all 84 lumen targets across the range of diameters explored are shown in Figure 4. Detectability was consistently higher for higher dose levels and for AIDR in comparison to FBP for a fixed resolution mode. This is expected given the lower image noise for higher dose values and for AIDR in comparison to FBP.[24] For the smaller lumen diameters (approximately 1–5 mm), the detectability was generally higher for HR than for NR as shown in Figure 5. The data suggests a decreasing linear trend in the ratio of d'_{det} values and the slope of this linear trend for 14 mGy (Figure 5a and 5b) is higher for the most peripheral location (R_C) in comparison to the more central locations (R_A and R_B). The lumen-diameter threshold for which there is an expected advantage for HR mode ($D_{HR>NR}$) using FBP-FC18 at 14 mGy was 1.6 mm [95% confidence interval: 0.1, 3.0], 2.7 mm [1.5,3.9], and 4.0 mm [4.0, 4.1] for R_A, R_B, and R_C, respectively. For AIDR-FC18 at 14 mGy the $D_{HR>NR}$ values were 4.20 mm [2.9,5.5], 6.8 mm [4.5,9.1], and 4.9 mm [4.9, 5.0] for R_A, R_B, and R_C, respectively. When the SSDE is increased to 21 mGy (Figure 5c and 5d), the $D_{HR>NR}$ estimations are more consistent across the scanner FOV, generally higher in magnitude, and the error in the estimation is lower. For FBP-FC18 at 21 mGy the $D_{HR>NR}$ values were 4.30 mm [4.2,4.3], 4.3 mm [4.3, 4.3], and 4.3 mm [4.3, 4.3] for R_A, R_B, and R_C, respectively. When using AIDR-FC18 at 21 mGy the most pronounced advantage for HR mode was observed with $D_{HR>NR}$ values of 7.1 mm [7.0,7.1], 7.0 mm [6.9, 7.0], and 6.8 mm [6.8, 6.9] for R_A, R_B, and R_C, respectively.

Figure 6a shows detection performance for HR mode as a function of lumen diameter for 21 mGy SSDE and the three different standard Body reconstruction protocols. NR was not included in this figure as AiCE is only available in HR mode. AiCE-STD resulted in higher detectability compared with AIDR-FC18 and FBP-FC18 – a consequence of the superior resolution and noise suppression for AiCE-STD as shown in previous studies.[31,32] For a 6 mm lumen diameter, the detectability was 48% and 18% higher for AiCE-STD in comparison to FBP-FC18 and AIDR-FC18, respectively. Similar trends are observed for a 2 mm lumen with 30% and 9% higher detectability for AiCE-STD in comparison to FBP-FC18 and AIDR-FC18, respectively. AiCE-STR results in moderate improvements over AiCE-STD for the detection task at 14 mGy SSDE as shown in Figure 6b. FBP-FC18 at 14 mGy SSDE (results not shown in Figure 6b) performed uniformly worse than AIDR-FC18 which is consistent with the results shown for 21 mGy.

Figure 7 shows detection performance for HR mode at 21 mGy SSDE and for lumens located at radial distances of 1.9 cm (R_A), 3.8 cm (R_B), and 6.4 cm (R_C) from the central axis of the phantom. Significantly higher performance (i.e., no overlap in 95% confidence interval) was observed for R_c in comparison to R_A for lumen diameters of 6.3 mm and 7.1 mm. This observation indicates an improvement in detection performance at the periphery of the phantom for the largest lumen diameters compared. Similar trends were observed for AiCE-STD at 14 mGy.

3.2. Size Discrimination

Size discrimination performance for different nominal diameters (2.95 mm to 10.08 mm) and stenosis severities (50% vs. 60% [50/60%], 50/70%, and 50/80%) are shown in Figure

Author Manuscript Author Manuscript Author Manuscript Author Manuscript

8. The linear relationship observed for d'_{dis} as a function of nominal diameter shows that discrimination performance scales with the nominal size of the lumen. Consistent with the detection task, we see an overall increase with AIDR-FC18 in comparison to FBP-FC18 and an increase with higher SSDE for all d'_{dis} results. Discrimination performance is consistently higher for larger differences in stenosis (e.g., 50/80% vs. 50/60%).

Looking specifically at the ratio of d'_{dis} for HR and NR (Figure 9), the ratio is highest for the smallest nominal diameters and for 50/60% compared with 50/80%. For example, averaged across the 5 nominal diameters, d'_{dis} for HR is 25%, 20%, and 17% greater than NR for 50/60%, 50/70%, and 50/80%, respectively, for AIDR-FC18 at 21 mGy SSDE (Figures 9d and 9h). Higher discrimination performance is observed for HR in comparison to NR at 21 mGy SSDE when using AIDR-FC18 across a range of nominal diameters and stenosis severity differences.

Figure 10 shows d'_{dis} results for HR mode comparing different reconstruction algorithms and plotted separately for different stenosis severity comparisons. For 21 mGy SSDE and the smallest difference in stenosis severity, discrimination performance for AiCE-STD is significantly higher (no overlapping error bars) than AIDR-FC18 for all nominal diameters investigated except the smallest diameter of 2.95mm (Figure 10a). AiCE-STD performance for 50/80% is significantly higher than AIDR-FC18 across all nominal diameters investigated (Figure 10b). With a lower dose level of 14 mGy SSDE (Figure 10c-d), AiCE-STR offers minimal improvements over AiCE-STD except for 50/80% stenosis differences for the largest nominal diameter of 10.08 mm (Figure 10d).

Figure 11 compares size discrimination performance (d'_{dis}) for AiCE-STD at 21 mGy SSDE. For small differences in stenosis (50/60%) size discrimination performance was consistent across position throughout the phantom except for nominal diameters of 7.14 mm and 10.08 mm. When comparing 50% vs. 80% stenoses, significant differences were observed for nominal diameters of 5.04 mm, 7.14 mm, and 10.08 mm. Similar trends were observed for AiCE-STD at 14 mGy.

4. DISCUSSION

Detectability estimations were above the Rose criterion ($d'_{det} \geq 5$) for all combinations compared except FBP-FC18 and AIDR-FC18 with 14 mGy SSDE for the smallest lumen diameters. The Rose criterion[33] serves as a simple measure of how visible the iodine-enhanced holes in the acrylic background are in the reconstructed CT images. This criterion is commonly used as a performance metric in noise-limited uniform backgrounds – consistent with its use here. The overall high detectability is expected given the relatively high contrast and dose used in this work. The data indicates that there is a lumen-diameter threshold above which HR no longer provides higher detection than NR mode. Figure 3b shows that signal amplitudes are concentrated at lower spatial frequencies for detection tasks. However, when the detection target is small enough (less than ~5 mm lumen diameter), there is sufficient high-frequency content to confer an advantage for HRCT as indicated by the results in Figure 5.

Author Manuscript Author Manuscript Author Manuscript Author Manuscript

Scanner performance for a size discrimination task was found to improve as nominal lumen diameter increases and for larger differences in stenosis severity as shown in Figure 8. AiCE outperforms the other two reconstruction algorithms compared (AIDR and FBP) particularly for larger nominal diameters and stenosis severity differences as shown in Figure 10. Even though the lowest discrimination performance is seen when comparing 50% vs. 60% stenosis (i.e., small differences in stenosis severity), the HR to NR mode ratio is highest for this case. This result is attributed to the increase in spatial resolution for HR mode which is advantageous for the discrimination task given the broad range of spatial frequencies in the differences signal as shown in Figure 3d.

As mentioned above, the detection of a high contrast disk posed in this study results in overall high detectability and therefore one could argue that detection (in the context of parameters investigated in this study) is not a task that needs improvements. We included detection to show that there is less of a proportional improvement in this task than there is for the discrimination task when comparing HR and NR modes. This observation is made clear when comparing the results presented in Figures 5 and 9.

Improvements in detection and discrimination performance were observed for the larger lumen targets at the periphery of the phantom compared to the center. Azimuthal blur resulting from the motion of the gantry increases as the location moves farther away from the isocenter and therefore we expect a decrease in resolution at the periphery of the scanner. However, given the range of radial distances investigated (1.9 cm to 6.4 cm), the differences in resolution are relatively small as detailed previously.[30] The observed increase in detection and discrimination performance for larger lumen diameters at the periphery of the phantom can be attributed to the higher image noise present at the center of the phantom compared to the periphery – a well-known phenomenon resulting from the relatively higher attenuation of x-rays passing through the phantom center.

This study aimed to compare detection and size discrimination performance using high resolution and normal resolution modes on the same system. It has been shown that the normal resolution mode on the Precision CT scanner performs somewhat worse than a comparable normal resolution system by the same vendor (Aquilion One Genesis, Canon Medical Systems Corporation).[34] While it would have been interesting to compare the results presented in this work with a comparable normal resolution system, we do not have access to such a system and therefore making these comparisons was not possible.

The detection templates used in this study were synthesized using the known properties of the holes, the measured HU values of the iodine and acrylic in images reconstructed using FBP, and the measured MTFs for all the different reconstruction algorithm/kernel combinations utilized. It is well understood that non-linear CT reconstruction algorithms, such as AIDR and AiCE employed in this study, could have an effect on the contrast of local features. However, these differences in contrast were not explicitly modeled in this work as the HU values used in the detection template were measured only using FBP. Despite this limitation, previously-reported work[34] has shown <3% deviation in CT numbers between HR and NR modes on the Precision system for Acrylic and Teflon materials, therefore the

Author Manuscript Author Manuscript Author Manuscript Author Manuscript

differences presented in this work when comparing these different resolution modes should still be valid.

The size discrimination task presented in this work is a simplified model for the clinical task of distinguishing visible size differences, but has been shown to be similar to a human observers processing of physical size differences.[14] We therefore anticipate that the general findings presented in this study for the discrimination task will translate well to human observer performance.

5. CONCLUSION

The high-resolution mode was found to provide significantly higher detection than NR mode on a high-resolution CT scanner for the smallest diameter investigated (1.32 mm), and the best performance in these comparisons were for AIDR-STD-FC18 at 21 mGy SSDE. For the task of size discrimination, it was found that HR mode outperforms NR mode across the range of nominal diameters and stenosis severity differences for AIDR-STD-FC18 at 21 mGy SSDE. Discrimination performance was higher for larger nominal diameters and larger differences in stenosis severity. This improvement for size discrimination using HR is especially true for smaller differences in stenoses (50% vs. 60%) which are important to distinguish for the clinical decision on how to treat patients with luminal stenoses. A deep learning-based reconstruction algorithm (AiCE), only available for HR mode, outperforms all other reconstruction algorithms and provides the highest detection and discrimination performance. We find high-resolution CT to be advantageous for the detection of smaller simulated lumen diameters (< 5 mm) and is more generally beneficial for discrimination tasks which inherently involve information at higher frequencies.

ACKNOWLEDGEMENTS

The authors would like to thank Dr. Elliot R. McVeigh (UC San Diego) for his insight and helpful discussions regarding the phantom design. We would also like to thank Dr. Kirsten Boedeker and Daniel W. Shin (Canon Medical Systems Inc.) for stimulating discussions on the topic of size discrimination.

REFERENCES

1. van den Wijngaard IR, Holswilder G, van Walderveen MA, et al. Treatment and imaging of intracranial atherosclerotic stenosis: current perspectives and future directions. Brain Behav. 2016;6(11):e00536. [PubMed: 27843693]
2. Lao D, Parasher PS, Cho KC, Yeghiazarians Y. Atherosclerotic renal artery stenosis--diagnosis and treatment. Mayo Clin Proc. 2011;86(7):649–657. [PubMed: 21719621]
3. North American Symptomatic Carotid Endarterectomy Trial C, Barnett HJM, Taylor DW, et al. Beneficial effect of carotid endarterectomy in symptomatic patients with high-grade carotid stenosis. N Engl J Med. 1991;325(7):445–453. [PubMed: 1852179]
4. MRC European Carotid Surgery Trial: interim results for symptomatic patients with severe (70–99%) or with mild (0–29%) carotid stenosis. European Carotid Surgery Trialists' Collaborative Group. Lancet. 1991;337(8752):1235–1243. [PubMed: 1674060]
5. Bartlett ES, Walters TD, Symons SP, Fox AJ. Carotid stenosis index revisited with direct CT angiography measurement of carotid arteries to quantify carotid stenosis. Stroke. 2007;38(2):286–291. [PubMed: 17170356]
6. Bartlett ES, Walters TD, Symons SP, Fox AJ. Quantification of carotid stenosis on CT angiography. AJNR Am J Neuroradiol. 2006;27(1):13–19. [PubMed: 16418349]

Author Manuscript Author Manuscript Author Manuscript Author Manuscript

7. Villablanca JP, Rodriguez FJ, Stockman T, et al. MDCT angiography for detection and quantification of small intracranial arteries: comparison with conventional catheter angiography. AJR Am J Roentgenol. 2007;188(2):593–602. [PubMed: 17242273]
8. Bash S, Villablanca JP, Jahan R, et al. Intracranial vascular stenosis and occlusive disease: evaluation with CT angiography, MR angiography, and digital subtraction angiography. AJNR Am J Neuroradiol. 2005;26(5):1012–1021. [PubMed: 15891154]
9. Wardlaw JM, Stevenson MD, Chappell F, et al. Carotid artery imaging for secondary stroke prevention: both imaging modality and rapid access to imaging are important. Stroke. 2009;40(11):3511–3517. [PubMed: 19729602]
10. Saxena A, Ng EYK, Lim ST. Imaging modalities to diagnose carotid artery stenosis: progress and prospect. Biomed Eng Online. 2019;18(1):66. [PubMed: 31138235]
11. Howell SJ. Carotid endarterectomy. Br J Anaesth. 2007;99(1):119–131. [PubMed: 17556351]
12. Rothwell PM, Eliasziw M, Gutnikov SA, et al. Analysis of pooled data from the randomised controlled trials of endarterectomy for symptomatic carotid stenosis. Lancet. 2003;361(9352):107–116. [PubMed: 12531577]
13. Seltzer SE, Swensson RG, Judy PF, Nawfel RD. Size discrimination in computed tomographic images. Effects of feature contrast and display window. Invest Radiol. 1988;23(6):455–462. [PubMed: 3403205]
14. Judy PF, Swensson RG. Size discrimination of features on CT images. Paper presented at: Application of Optical Instrumentation in Medicine XIV and Picture Archiving and Communication Systems1986.
15. Tapiovaara MJ, Wagner RF. SNR and noise measurements for medical imaging: I. A practical approach based on statistical decision theory. Phys Med Biol. 1993;38(1):71–92. [PubMed: 8426870]
16. Richard S, Siewerdsen JH. Comparison of model and human observer performance for detection and discrimination tasks using dual-energy x-ray images. Med Phys. 2008;35(11):5043–5053. [PubMed: 19070238]
17. Krejza J, Arkuszewski M, Kasner SE, et al. Carotid artery diameter in men and women and the relation to body and neck size. Stroke. 2006;37(4):1103–1105. [PubMed: 16497983]
18. Zanoli L, Rastelli S, Marcantoni C, et al. Renal artery diameter, renal function and resistant hypertension in patients with low-to-moderate renal artery stenosis. J Hypertens. 2012;30(3):600–607. [PubMed: 22241139]
19. Dodge JT Jr., Brown BG, Bolson EL, Dodge HT. Lumen diameter of normal human coronary arteries. Influence of age, sex, anatomic variation, and left ventricular hypertrophy or dilation. Circulation. 1992;86(1):232–246. [PubMed: 1535570]
20. Bae KT. Intravenous contrast medium administration and scan timing at CT: considerations and approaches. Radiology. 2010;256(1):32–61. [PubMed: 20574084]
21. Hinzpeter R, Eberhard M, Gutjahr R, et al. CT Angiography of the Aorta: Contrast Timing by Using a Fixed versus a Patient-specific Trigger Delay. Radiology. 2019;291(2):531–538. [PubMed: 30835189]
22. Saade C, Deeb IA, Mohamad M, Al-Mohiy H, El-Merhi F. Contrast medium administration and image acquisition parameters in renal CT angiography: what radiologists need to know. Diagn Interv Radiol. 2016;22(2):116–124. [PubMed: 26728701]
23. Morotti A, Romero JM, Jessel MJ, et al. Phantom-based standardization of CT angiography images for spot sign detection. Neuroradiology. 2017;59(9):839–844. [PubMed: 28730267]
24. Hernandez AM, Shin DW, Abbey CK, et al. Validation of synthesized normal-resolution image data generated from high-resolution acquisitions on a commercial CT scanner. Med Phys. 2020;47(10):4775–4785. [PubMed: 32677085]
25. Boone JM, Strauss KJ, Cody DD, McCollough CH, McNitt-Gray MF, Toth TL. Size-Specific Dose Estimates (SSDE) in Pediatric and Adult Body CT Examinations: The Report of AAPM Task Group 204. AAPM Report. 2011.
26. Kanal KM, Butler PF, Sengupta D, Bhargavan-Chatfield M, Coombs LP, Morin RL. U.S. Diagnostic Reference Levels and Achievable Doses for 10 Adult CT Examinations. Radiology. 2017;284(1):120–133. [PubMed: 28221093]

Author Manuscript Author Manuscript Author Manuscript Author Manuscript

27. Boone JM, Strauss KJ, Hernandez AM, et al. Size-Specific Dose Esimate (SSDE) for Head CT: The Report of AAPM Task Group 293. AAPM Report. 2019.
28. Myers KJ, Barrett HH, Borgstrom MC, Patton DD, Seeley GW. Effect of noise correlation on detectability of disk signals in medical imaging. J Opt Soc Am A. 1985;2(10):1752–1759. [PubMed: 4056949]
29. Burgess AE. Statistically defined backgrounds: performance of a modified nonprewhitening observer model. J Opt Soc Am A Opt Image Sci Vis. 1994;11(4):1237–1242. [PubMed: 8189286]
30. Hernandez AM, Wu P, Mahesh M, Siewerdsen JH, Boone JM. Location and direction dependence in the 3D MTF for a high-resolution CT system. Med Phys. 2021;48(6):2760–2771. [PubMed: 33608927]
31. Greffier J, Dabli D, Frandon J, et al. Comparison of two versions of a deep learning image reconstruction algorithm on CT image quality and dose reduction: A phantom study. Med Phys. 2021;48(10):5743–5755. [PubMed: 34418110]
32. Urikura A, Yoshida T, Nakaya Y, Nishimaru E, Hara T, Endo M. Deep learning-based reconstruction in ultra-high-resolution computed tomography: Can image noise caused by high definition detector and the miniaturization of matrix element size be improved? Phys Med. 2021;81:121–129. [PubMed: 33453504]
33. Rose A. The sensitivity performance of the human eye on an absolute scale. J Opt Soc Am. 1948;38(2):196–208. [PubMed: 18901781]
34. Oostveen LJ, Boedeker KL, Brink M, Prokop M, de Lange F, Sechopoulos I. Physical evaluation of an ultra-high-resolution CT scanner. Eur Radiol. 2020;30(5):2552–2560. [PubMed: 32040726]

Author Manuscript Author Manuscript Author Manuscript Author Manuscript

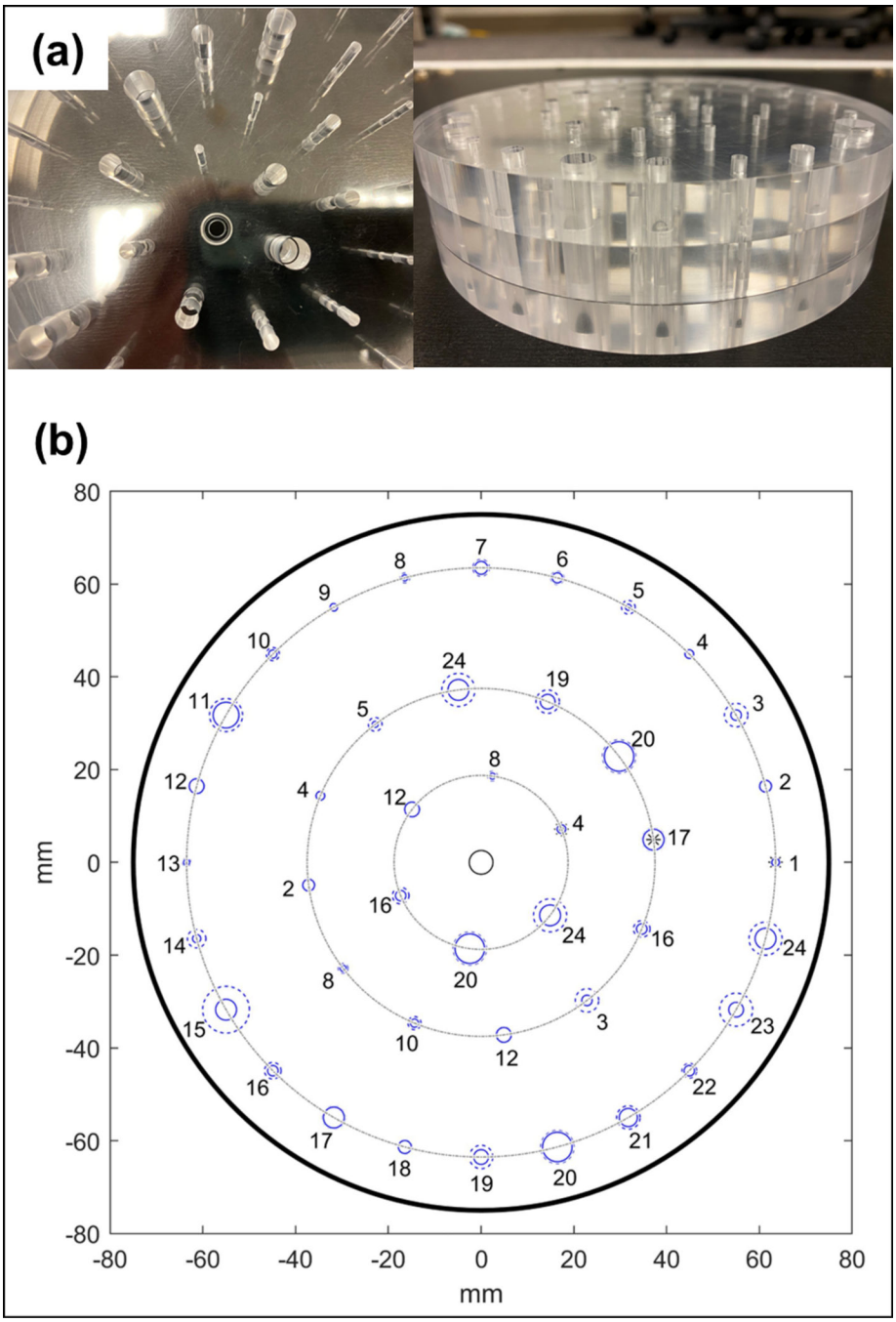

Figure 1.

Photographs of the three machined acrylic cylinders comprising the stenotic lesion phantom (a) and a schematic showing the indexing and relative locations of the array of holes at three different radial locations from the phantom center (R_A, R_B, and R_C). Table 1 details each hole diameter and simulated stenosis severity for the indexing showing in (b).

Author Manuscript Author Manuscript Author Manuscript Author Manuscript

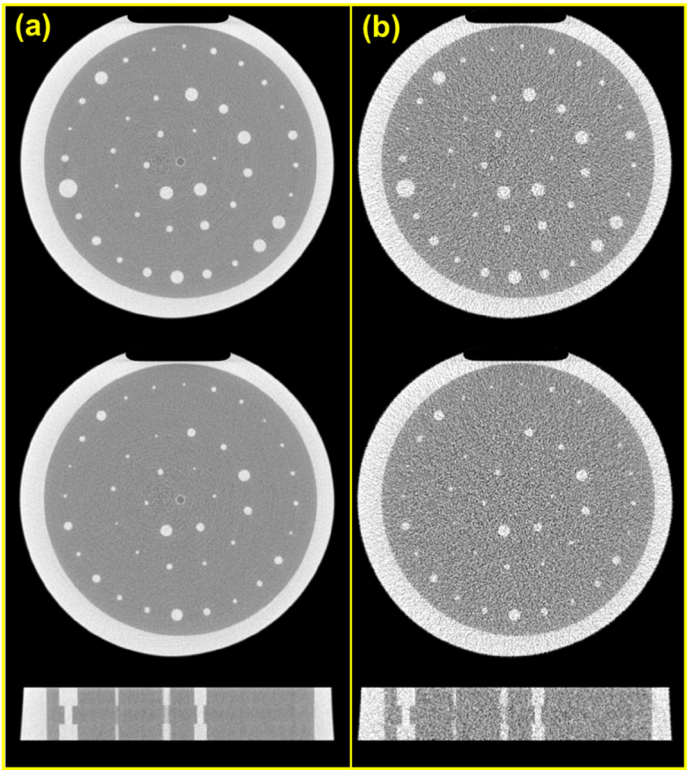

Figure 2.

Axial slices through the outer (top row) and central modules (central row) are shown along with a sagittal slice (bottom row) through the stenosis phantom. The images represent the ensemble average of 30 repeat scans (a) and a single scan (b) for FBP reconstruction with the FC18 kernel.

Author Manuscript Author Manuscript Author Manuscript Author Manuscript

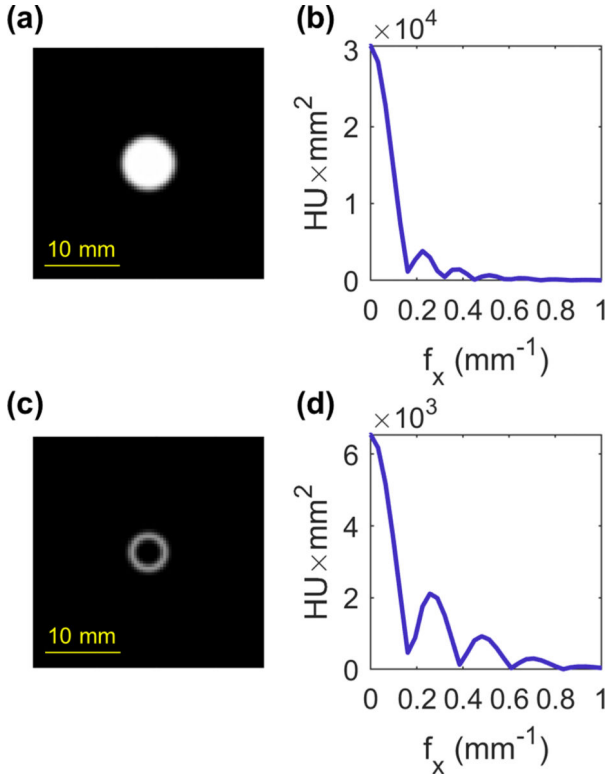

Figure 3.

Examples of the difference signal (a,c) and corresponding Fourier transform (b,d) are shown for the detection (a,b) and discrimination tasks (c,d). The lumen diameter is 7.14 mm for the detection task and the discrimination task represents the 50% stenosis (5.05 mm lumen diameter) and 70% stenosis (3.91 mm) for a nominal 7.14 mm diameter lumen.

Author Manuscript Author Manuscript Author Manuscript Author Manuscript

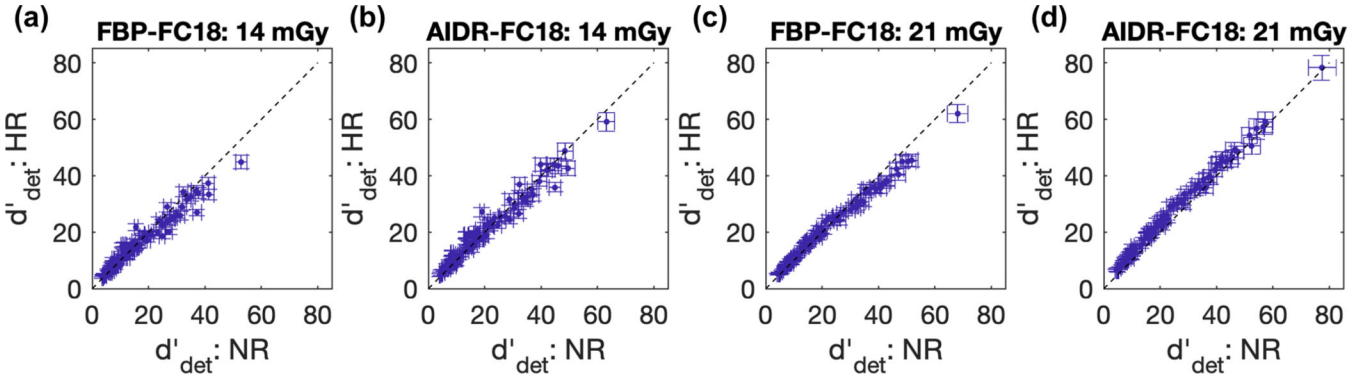

Figure 4.

Detection performance (d'_{det}) results are shown for FBP-FC18; 14 mGy SSDE (a) AIDR-FC18; 14 mGy (b), FBP-FC18; 21 mGy (c), and AIDR-FC18; 21 mGy (d). Estimations are plotted for NR mode (y-axis) and HR mode (x-axis) across all 84 lumen targets along with the line of identity (dashed line). The x and y error bars indicate the 95% confidence interval derived from bootstrapping across the 30 repeat scans.

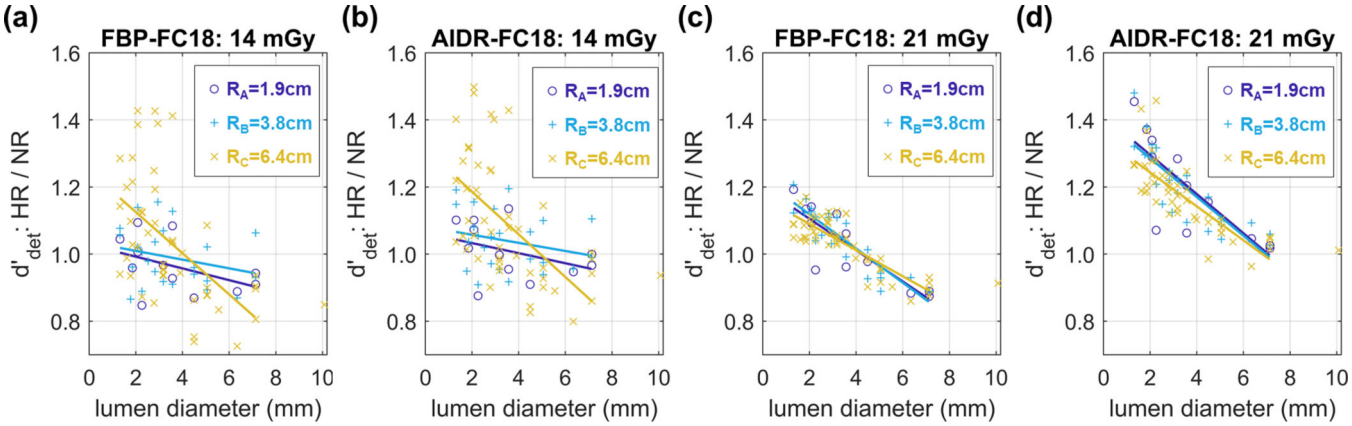

Figure 5.

Detection performance (d'_{det}) results shown as a ratio of HR to NR for lumens located at three different radial locations ($R_{A\text{-}C}$) from the central axis of the phantom. The linear fit was calculated for all data points except the 10.08 mm lumen diameter at the R_C radial location.

Author Manuscript Author Manuscript Author Manuscript Author Manuscript

Author Manuscript Author Manuscript Author Manuscript Author Manuscript

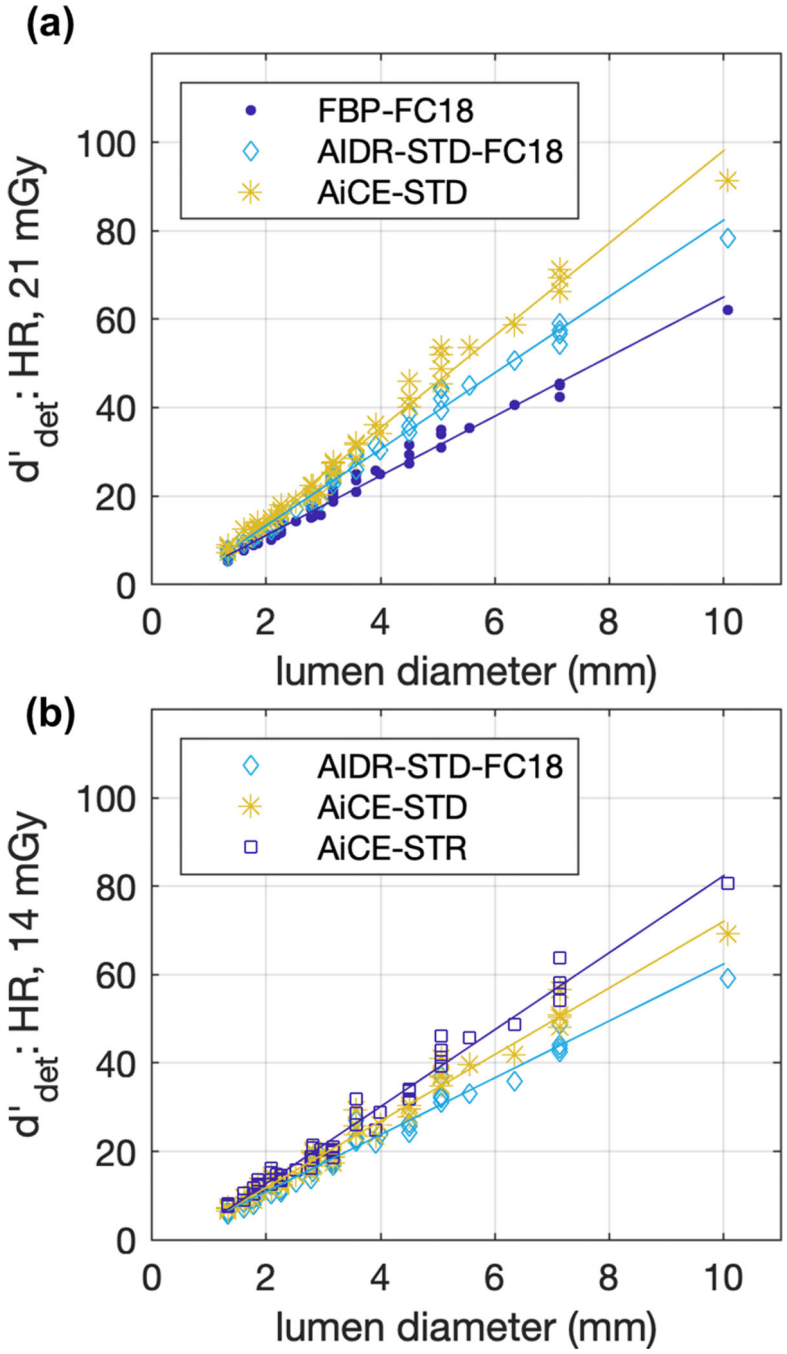

Figure 6.

Detection performance (d'_{det}) plotted for HR mode at 21 mGy SSDE (a) and 14 mGy SSDE (b) for all 48 lumen targets (24 for outer disk and 24 for central disk) in the outer radial location (R_C).

Author Manuscript Author Manuscript Author Manuscript Author Manuscript

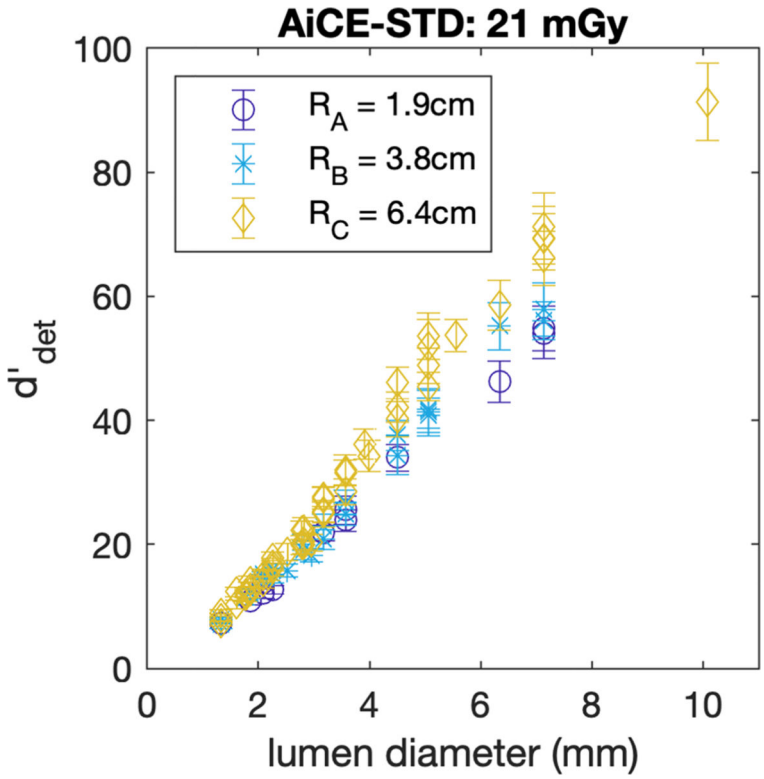

Figure 7.

Detection performance (d'_{det}) plotted for HR mode at 21 mGy SSDE for lumens located at the three different radial locations of 1.9 cm (R_A), 3.8 cm (R_B), and 6.4 cm (R_C) from the central axis of the phantom. The error bars indicate the 95% confidence interval derived from bootstrapping across the 30 repeat scans.

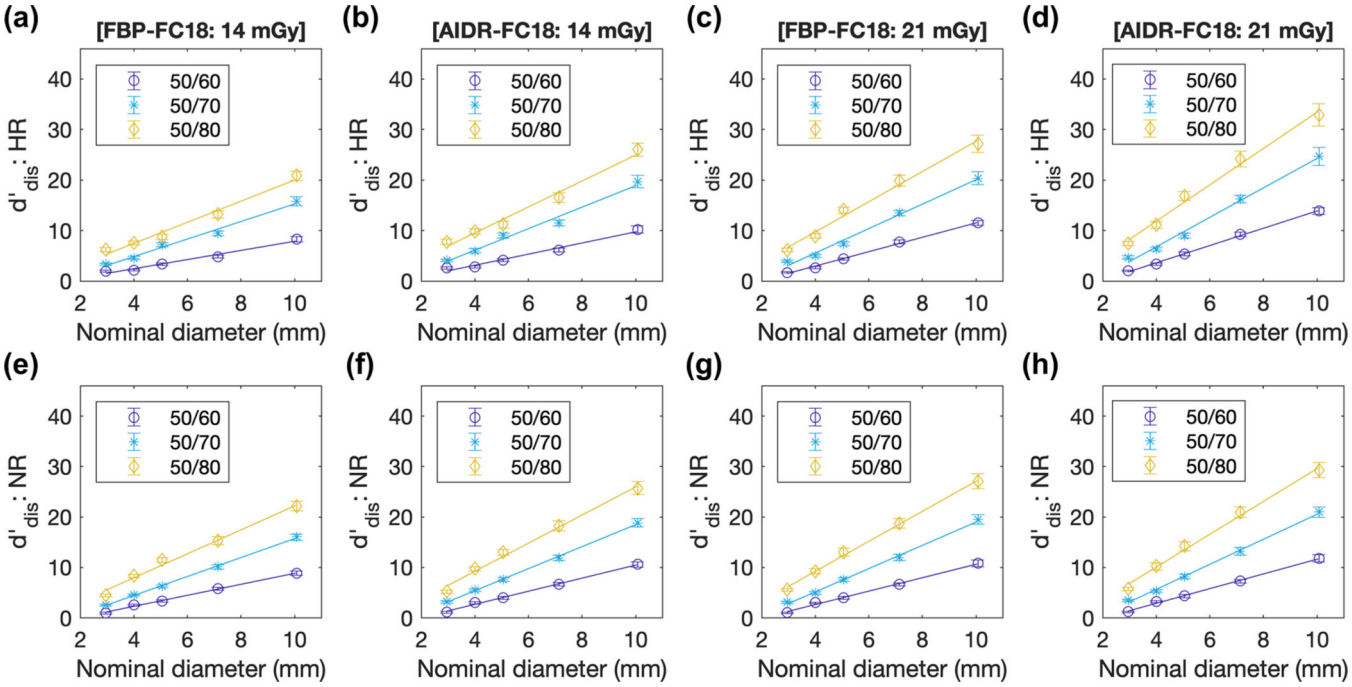

Figure 8.

Size discrimination (d'_{dis}) results are plotted for HR mode (a-d) and NR mode (e-h) for FBP-FC18; 14 mGy SSDE (a,e) AIDR-FC18; 14 mGy (b,f), FBP-FC18; 21 mGy (c,g), and AIDR-FC18; 21 mGy (d,h) across all 24 lumen difference targets in the outer radial location (R_C). Resulted are plotted separately for 50% vs. 60% stenoses (50/60), 50/70, and 50/80%. The y-axis error bars indicate the 95% confidence interval derived from bootstrapping across the 30 repeat scans.

Author Manuscript Author Manuscript Author Manuscript Author Manuscript

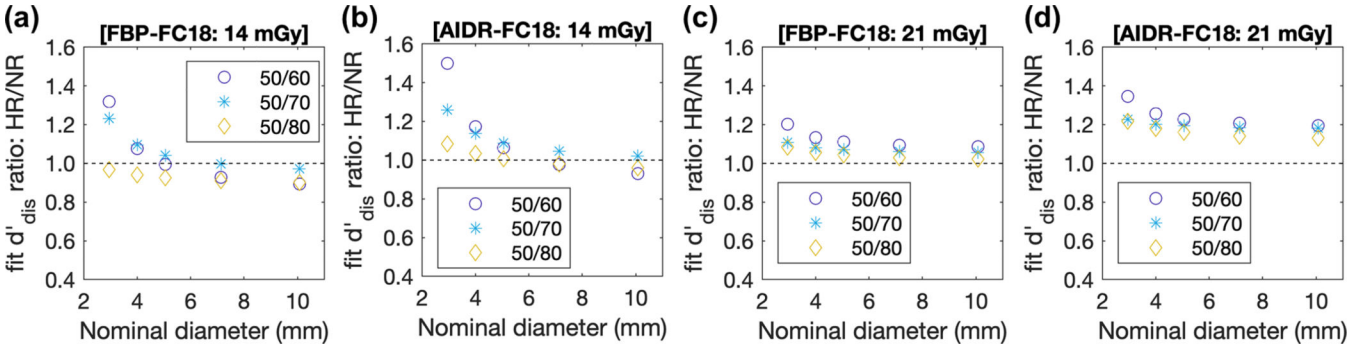

Figure 9.

Size discrimination (d'_{dis}) results are plotted as a ratio of the fitted data (Figure 6) for HR to NR mode across all 24 lumen difference targets in the outer radial location (R_C).

Author Manuscript Author Manuscript Author Manuscript Author Manuscript

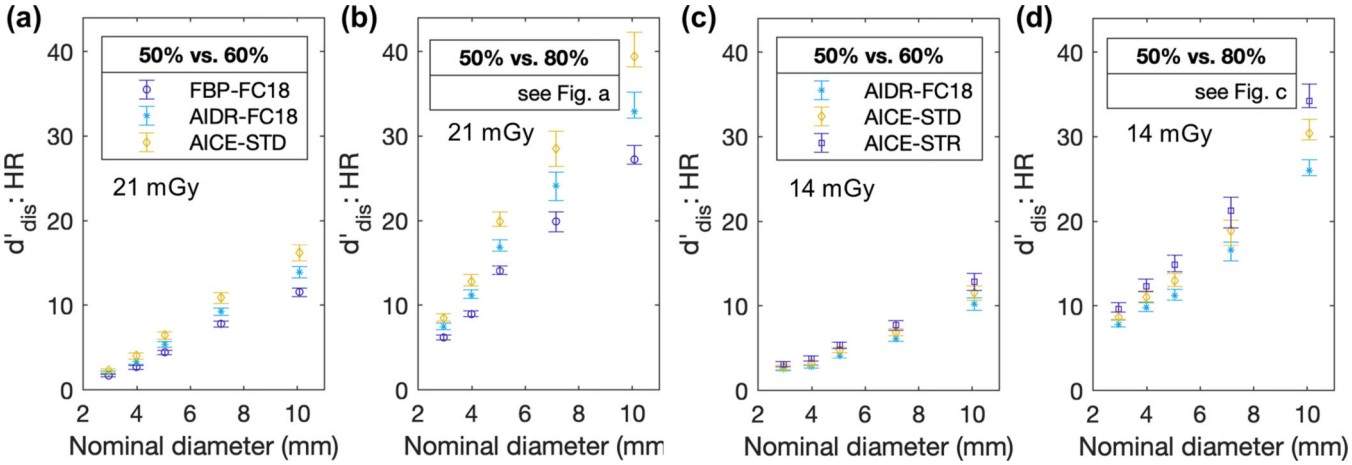

Figure 10.

Size discrimination (d'_{dis}) results are plotted for HR mode at 21 mGy SSDE (a,b) and 14 mGy SSDE (c,d) across various stenosis differences in the outer radial location (R_C). The error bars indicate the 95% confidence interval derived from bootstrapping across the 30 repeat scans.

Author Manuscript Author Manuscript Author Manuscript Author Manuscript

Author Manuscript Author Manuscript Author Manuscript Author Manuscript

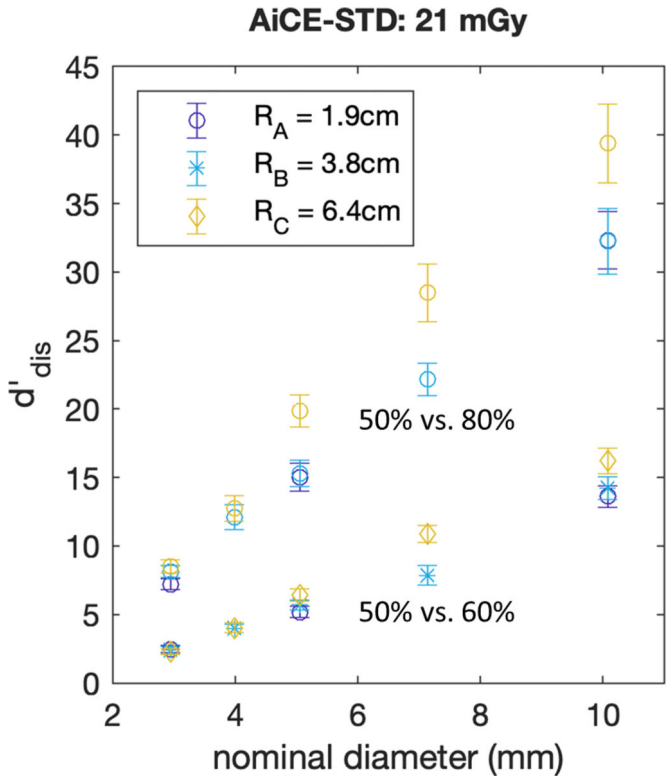

Figure 11.

Discrimination performance (d'_{dis}) plotted for HR mode at 21 mGy SSDE for lumens located at the three different radial locations of 1.9 cm (R_A), 3.8 cm (R_B), and 6.4 cm (R_C) from the central axis of the phantom. The error bars indicate the 95% confidence interval derived from bootstrapping across the 30 repeat scans.

Author Manuscript Author Manuscript Author Manuscript Author Manuscript

Table 1.

Size specifications for the 24 unique hole pairs in the stenosis phantom. The hole pairs are organized by the nominal simulated-lumen diameters of 3, 4, 5, 7, and 10 mm (rounded to the nearest 0.1 mm) and then by stenosis percentage for the outer and central modules of the phantom. The largest radial distance from the phantom center (R_C = 6.4 cm) contains all 24 hole pairs.

Hole Index	$D_{nominal}$ (mm)	D_{outer} (mm)	$Stenosis_{outer}$ (%)	$D_{central}$ (mm)	$Stenosis_{central}$ (%)
9	2.95	1.85	60.4	1.61	70.0
13	“	1.85	60.4	1.32	79.9
1	“	2.08	50.0	1.61	70.0
4[a,b]	“	2.08	50.0	1.85	60.4
8[a,b]	“	2.08	50.0	1.32	79.9
5[b]	“	2.95	0.0	1.32	79.9
2[b]	3.99	2.82	50.0	2.53	59.8
6	“	2.82	50.0	2.18	70.0
10[b]	“	2.82	50.0	1.78	80.1
14	“	3.99	0.0	1.78	80.1
18	5.05	3.17	60.5	2.78	69.8
22	“	3.17	60.5	2.26	80.0
7	“	3.57	50.1	2.78	69.8
12[a,b]	“	3.57	50.1	3.17	60.5
16[a,b]	“	3.57	50.1	2.26	80.0
3[b]	“	5.05	0.0	2.26	80.0
17[b]	7.14	5.05	49.9	4.50	60.4
19[b]	“	5.05	49.9	3.17	80.2
21	“	5.05	49.9	3.91	70.0
23	“	7.14	0.0	3.17	80.2
11	10.08	7.14	49.9	5.56	69.6
20[a,b]	“	7.14	49.9	6.35	60.3
24[a,b]	“	7.14	49.9	4.50	80.1
15	“	10.08	0.0	4.50	80.1

[a] Hole index repeated for radial location R_A (1.9 cm from the phantom center)

[b] Hole index repeated for radial location R_B (3.8 cm from the phantom center)